Check for updates

Enhanced luminescence properties of Ca$_{1+x}$Sr$_{2-x}$Al$_2$O$_6$:Eu^{3+} (0 ≤ x ≤ 1) red phosphors based on composition modulation†

Biao Shen, Jianghang Xu, Qinan Mao* and Jiasong Zhong [ID] *

A series of solid solution Ca$_{1+x}$Sr$_{2-x}$Al$_2$O$_6$:Eu^{3+} (0 ≤ x ≤ 1) phosphors has been successfully synthesized *via* a high-temperature solid-state method. The phase structures, photoluminescence performances, and fluorescence lifetimes, as well as the thermal stability properties, have been systematically investigated. All of the samples possess a cubic structure system and belong to the *Pa*$\bar{3}$(205) space-group. Owing to the $^5D_0 \rightarrow \, ^7F_2$ transition of the Eu^{3+} ions, the photoluminescence emission (PL) spectra demonstrate a strong red emission band at around 612 nm. As the Sr^{2+} ions have been substituted by Ca^{2+} ions in the CaSr$_2$Al$_2$O$_6$:Eu^{3+} composition, the luminous intensities are gradually enhanced owing to the average bond lengths of Ca–O, Sr/Ca–O, and Sr–O, which are shorter. In addition, the PL intensities at 423 K for the CaSr$_2$Al$_2$O$_6$:0.02Eu^{3+}, Ca$_{1.5}$Sr$_{1.5}$Al$_2$O$_6$:0.02Eu^{3+}, and Ca$_2$SrAl$_2$O$_6$:0.02Eu^{3+} phosphors retain 84.5%, 76.1%, and 75.7% of their intensities, respectively, compared with their initial intensities at 303 K. The results demonstrate that high-performance Eu^{3+}-activated red-emitting phosphors can be obtained *via* cation substitution.

1. Introduction

In the last few decades, white light-emitting diodes (WLEDs) have been widely studied, owing to their typical advantages such as long lifetime, high luminous efficiency, small volume, high brightness, being environmentally friendly and having an excellent stability, and they are considered as the fourth generation of all-solid-state green lighting sources.[1–7] Currently, the most common way to fabricate commercial WLEDs is by combining a blue InGaN LED chip with a YAG:Ce^{3+} (Y$_3$Al$_5$O$_{12}$:Ce^{3+}) yellow-emitting phosphor.[8–11] Nonetheless, owing to the deficiency of the red-emitting component, the devices have some disadvantages, such as a high correlated color temperature (CCT) and a poor color rendering index (CRI).[12–14] Consequently, these WLEDs do not meet the requirements for indoor illuminations, which limit their further development as light sources in this field.[15–17] Therefore, in order to improve the CCT and CRI, more and more well-performing red-emitting phosphors have been studied.[18,19] However, compared with commercially available blue and green phosphors, many obvious shortcomings exist in red-emitting phosphors.[8,17,20] For instance, M$_2$Si$_5$N$_8$:Eu^{2+} (M = Ca, Sr and Ba) and Y$_2$O$_2$S:Eu^{3+} possess poor performances in terms of the chemical stability, luminescence efficiency and environmental protection (for example, the

production of sulfide gas).[20–22] Therefore, the development of a novel red-emitting phosphor at a low cost, that is non-polluting, has a superior stability, and satisfactory luminous efficiency is urgently needed to satisfy the requirements of warm WLEDs.[14,19]

In order to obtain a well performing red phosphor for use in WLEDs, the host lattice is one of the important factors.[23] In recent years, aluminate-based phosphors have been extensively used for their excellent properties, such as a good luminous efficiency, high CRI and wide excitation range.[24–26] For example, Ce^{3+}-doped Lu$_3$Al$_5$O$_{12}$ yellow phosphor and Eu^{2+}-doped SrAl$_2$O$_4$ green phosphor possess good luminescence performances.[27,28] Furthermore, compounds containing the M$_3$Al$_2$O$_6$ (M = Ca, Sr) structure have received significant attention owing to their particular crystal structure and excellent chemical stability.[15,24,29] In particular, there are several kinds of cation sites in the crystal structure of M$_3$Al$_2$O$_6$ with a low symmetry, which effectively enhance the intensity of the $^5D_0$–$^7F_2$ transition.[20] Additionally, the composition of the host structure can be adjusted by modifying the cations in the M site, and then improving the activator environment and luminescent properties.[30] It is well known that the Eu^{3+} ion is one of the most efficient red luminescent rare-earth activators, which always emit a bright red light with a high luminous efficiency.[12,14,31] In addition, the Eu^{3+} ions have two intense excitation peaks at approximately 393 nm ($^7F_0$–$^5L_6$) and 465 nm ($^7F_0$–$^5D_2$) in most host lattices, which are suitable for use in near-ultraviolet LED chips and blue LED chips.[21,32] Moreover, the Eu^{3+} ions possess strong red emission peaks at approximately 590 nm and 615 nm originating from their $^5D_0$–^7F_i (i = 1, 2) transitions.[3,33,34]

College of Materials and Environmental Engineering, Hangzhou Dianzi University, Hangzhou 310018, China. E-mail: maoqinan@hdu.edu.cn; jiasongzhong@hdu.edu.cn

In this work, a Eu^{3+}-doped $Ca_{1+x}Sr_{2-x}Al_2O_6$ ($0 \leq x \leq 1$) composite has been studied as a potential alternative to red-emitting phosphors. The luminous efficiency and thermal stability can be improved by adjusting the proportion of the Ca^{2+} and Sr^{2+} ions. In addition, $Ca_{1+x}Sr_{2-x}Al_2O_6$ has a cubic structure with a $Pa\bar{3}(205)$ space-group, which provides a suitable environment for Eu^{3+} ions. Furthermore, the ionic radius of the Eu^{3+} ions ($r = 0.947$ Å, CN = 6) is similar to that of Ca^{2+} ions ($r = 1.00$ Å, CN = 6) and Sr^{2+} ions ($r = 1.18$ Å, CN = 6), indicating the significant possibility of using the Eu^{3+} ion to replace the Ca^{2+} and Sr^{2+} sites in the $Ca_{1+x}Sr_{2-x}Al_2O_6$ host lattice. Hence, a series of $Ca_{1+x}Sr_{2-x}Al_2O_6$ ($0 \leq x \leq 1$) red phosphors have been synthesized using the solid-state reaction method. The crystal structures, morphologies and photoluminescence emission (PL) properties of the phosphor samples have been studied in detail. In addition, the concentration quenching and thermal stability have also been investigated.

2. Experimental section

2.1 Preparation of the samples

A series of $CaSr_2Al_2O_6:yEu^{3+}$ ($y = 0.005, 0.01, 0.02, 0.03, 0.04, 0.05$ and 0.10) and $Ca_{1+x}Sr_{2-x}Al_2O_6:0.02Eu^{3+}$ ($x = 0, 0.2, 0.4, 0.6, 0.8$ and 1.0) phosphors were successfully synthesized using a high-temperature solid-state method. $CaCO_3$ (99.99%), $SrCO_3$ (99.99%), Al_2O_3 (99.99%) and Eu_2O_3 (99.99%) were used as raw materials. First, these starting materials were weighed according to the stoichiometric ratio, and then mixed uniformly, and ground thoroughly for 30 min. After that, the compounds were placed into alumina crucibles and pre-sintered at 800 °C for 6 h in air. The phosphor samples were then reground for 20 min and calcined at 1250 °C for 5 h. Finally, the resulting powder samples were naturally cooled to room temperature in the furnace and ground again for further characterization.

2.2 Characterization

The phase purity information of the samples was characterized on a MiniFlex 600 X-ray diffractometer using Cu Kα ($\lambda = 1.5405$ Å) radiation. Scanning steps of $1°$ min^{-1} were used when scanning the 2θ range from $10°$ to $80°$. The crystal structure parameters were further analyzed and refined via the Rietveld method using the software program General Structure Analysis System (GSAS). The morphology was detected using scanning electron microscopy (SEM, FEI Apreo HiVac). The element compositions were studied using energy dispersive X-ray spectrometry (EDX), using a spectrometer attached to the SEM. X-ray photoelectron spectroscopy (XPS) analysis was carried out using the monochromatic Al Kα excitation source. The PL spectra, photoluminescence excitation (PLE) spectra and the luminescence decay curves of the prepared samples were measured on a spectrometer (UK, Edinburgh, FS5) using a continuous and pulsed xenon lamp (150 W) as the excitation source. The thermal quenching was studied from 303 to 503 K using PL equipment with a homemade temperature control system.

3. Results and discussion

3.1 Phase structures and morphology analysis

The crystal structure and occupation probability, as well as the phase purity of the $CaSr_2Al_2O_6:0.02Eu^{3+}$ and $Ca_2SrAl_2O_6:0.02Eu^{3+}$ samples were developed using the GSAS Rietveld refinement, as illustrated in Fig. 1. The crystallographic standard data cards of ICSD-520249($CaSr_2Al_2O_6$) and ICSD-520250($Ca_2SrAl_2O_6$) were employed as the initial structural model. The final refinement results for the $CaSr_2Al_2O_6:0.02Eu^{3+}$ and $Ca_2SrAl_2O_6:0.02Eu^{3+}$ samples, as well as their standard cell parameters, are presented in Table 1. Accordingly, the $CaSr_2Al_2O_6:0.02Eu^{3+}$ and $Ca_2SrAl_2O_6:0.02Eu^{3+}$ samples possess a cubic structure system with a space-group of $Pa\bar{3}(205)$. In addition, the unit cell volume of $CaSr_2Al_2O_6:0.02Eu^{3+}$ ($a = 15.456$ Å, $V = 3692.4$ Å^3) and $Ca_2SrAl_2O_6:0.02Eu^{3+}$ ($a = 15.380$ Å, $V = 3638.3$ Å^3) are smaller than those of pure $CaSr_2Al_2O_6$ ($a = 15.550$ Å, $V = 3760.0$ Å^3) and the $Ca_2SrAl_2O_6$ ($a = 15.408$ Å, $V = 3658.0$ Å^3) host, respectively. The shrinking of the unit cell volume further demonstrates that the Eu^{3+} ions have successfully moved into the host. It is well known that the percentage difference for the ion radius between
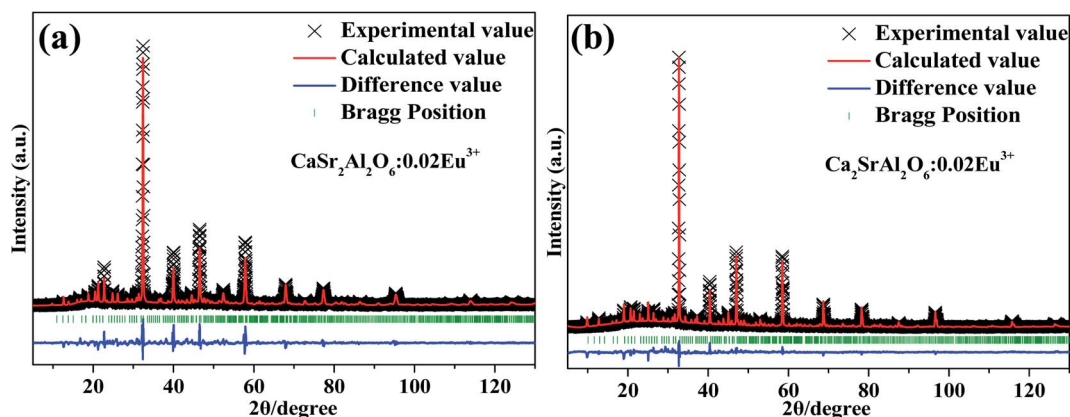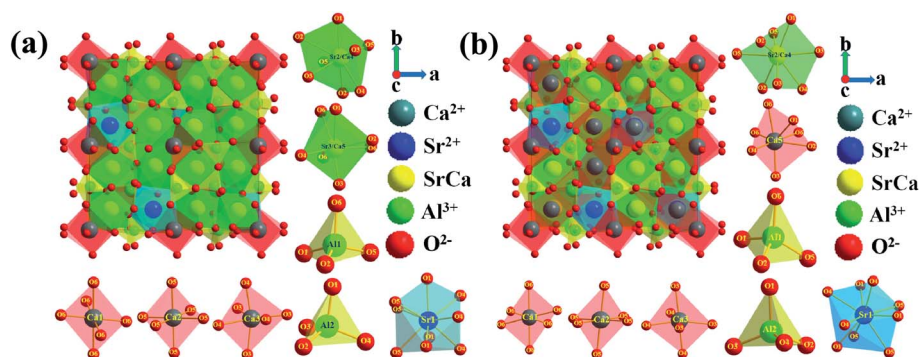

Fig. 1 XRD patterns based on the Rietveld refinement results for (a) $CaSr_2Al_2O_6:0.02Eu^{3+}$ and (b) $Ca_2SrAl_2O_6:0.02Eu^{3+}$ samples. The experimental values are shown by black crosses. The Rietveld calculated values and the difference curves are indicated with red and blue lines, respectively. The Bragg reflections are given as green short vertical lines.

Table 1 Structural parameters for the $CaSr_2Al_2O_6{:}0.02Eu^{3+}$ and $Ca_2SrAl_2O_6{:}0.02Eu^{3+}$ samples

	$CaSr_2Al_2O_6$	$CaSr_2Al_2O_6{:}0.02Eu^{3+}$	$Ca_2SrAl_2O_6$	$Ca_2SrAl_2O_6{:}0.02Eu^{3+}$
Crystal system	Cubic	Cubic	Cubic	Cubic
Space group	$Pa\bar{3}(205)$	$Pa\bar{3}(205)$	$Pa\bar{3}(205)$	$Pa\bar{3}(205)$
Units, Z	24	24	24	24
a (Å)	15.550	15.456	15.408	15.380
V (Å^3)	3760.0	3692.4	3658.0	3638.3
R_p (%)		10.05		8.01
R_{wp} (%)		13.53		11.24
R_E (%)		4.58		4.94
χ^2		8.718		5.187

Fig. 2 Unit cell crystal structures of (a) $CaSr_2Al_2O_6$, and (b) $Ca_2SrAl_2O_6$ with the coordination environments for Ca^{2+}, Sr^{2+}, and Al^{3+}.

the host and doped ions should be less than 30%.[8] As for Al^{3+} ions ($r = 0.39$ Å, CN = 4), Ca^{2+} ions ($r = 1.00$ Å, CN = 6) and Sr^{2+} ions ($r = 1.18$ Å, CN = 6), the values were calculated and found to be −142.82%, 5.3% and 19.7%, respectively. Therefore, there is no possibility of Eu^{3+} ions being doped into the Al^{3+} sites. Moreover, the unit cell crystal structure diagrams of the $CaSr_2Al_2O_6$ and $Ca_2SrAl_2O_6$ samples with the coordination environments of Ca^{2+}, Sr^{2+}, Al^{3+} are presented in Fig. 2. Obviously, there are six kinds of crystallographic sites for the Ca and Sr atoms in the three crystal structures, including Ca1, Ca2, Ca3, Sr2/Ca4, Sr3/Ca5 and Sr1 in $CaSr_2Al_2O_6$ and Ca1, Ca2, Ca3, Sr2/

Ca4, Ca5 and Sr1 in $Ca_2SrAl_2O_6$, respectively. The abundant octahedrons [CaO_6] consist of Ca^{2+} ions surrounded by six O^{2-}. In addition, the Sr1, Sr2/Ca4 and Sr3/Ca5 sites are coordinated with nine, eight and seven oxygen atoms, respectively. Among them, the polyhedral structures of the Ca and Sr atoms provide suitable conditions for the Ca^{2+} and Sr^{2+} ions, which can be easily replaced by Eu^{3+} ions.

The XRD patterns of the $CaSr_2Al_2O_6{:}yEu^{3+}$ (y = 0.005, 0.01, 0.02, 0.03, 0.04, 0.05 and 0.10) and $Ca_{1+x}Sr_{2-x}Al_2O_6{:}0.02Eu^{3+}$ (x = 0, 0.2, 0.4, 0.6, 0.8 and 1.0) samples were measured and are shown in Fig. 3a and S1a.† As the Eu^{3+} ions are doped into the
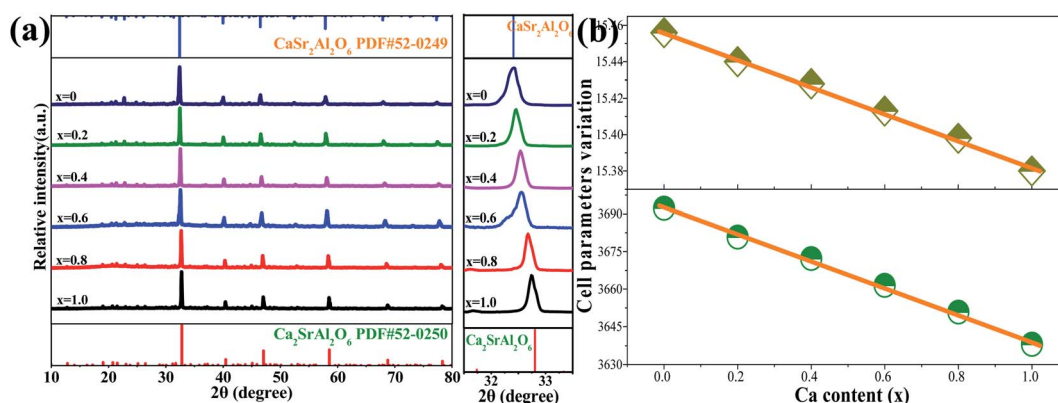
Fig. 3 (a) XRD patterns of $Ca_{1+x}Sr_{2-x}Al_2O_6{:}0.02Eu^{3+}$ (x = 0, 0.2, 0.4, 0.6, 0.8 and 1.0) samples and the corresponding enlarged XRD patterns in the range of 31.5° to 33.5°. (b) The variations of the lattice parameters (a and V) as a function of the Ca^{2+} content.

host or Sr^{2+} ions are substituted by Ca^{2+} ions, no other impurity phases can be observed. In addition, with the increasing Eu^{3+} concentration, the main diffraction peaks gradually shift towards the higher side of the angles, as presented in Fig. S1b.† Based on the Bragg equation ($2d \sin \theta = n\lambda$), in which d, λ and θ, respectively, correspond to interplanar crystal spacing, the wavelength of the X-ray and the diffraction angle, this phenomenon can be attributed to the Ca^{2+} or Sr^{2+} ions that are replaced by the Eu^{3+} ions. Thus, with the increasing concentration of Eu^{3+} ions, the interplanar crystal spacing (d) will decrease owing to the effective ionic radius of the Eu^{3+} ions ($r = 0.947$ Å, $CN = 6$) being smaller than those of the Ca^{2+} or Sr^{2+} ions. Similarly, the Sr^{2+} ions are gradually replaced by Ca^{2+} ones in the $Ca_{1+x}Sr_{2-x}Al_2O_6$:0.02Eu^{3+} ($x = 0$, 0.2, 0.4, 0.6, 0.8 and 1.0) samples, the main diffraction peaks shift to a larger angle value, as shown in Fig. 3a, which can be attributed to the larger Sr^{2+} ions, which are displaced by smaller Ca^{2+} ones. In addition, the variations in the cell parameter a and the unit cell volume V in the $Ca_{1+x}Sr_{2-x}Al_2O_6$:0.02Eu^{3+} samples have been demonstrated in Fig. 3b. Obviously, the lattice parameters present a linear decline owing to the enhancement of the Ca^{2+} contents, in which the a and V reduce from 15.456 to 15.380 Å and 3692.4 to 3638.3 Å^3, respectively. These results further confirm the substituted Ca^{2+} for the Sr^{2+} sites in the host lattice of $Ca_{1+x}Sr_{2-x}Al_2O_6$:0.02Eu^{3+}.

The morphology and composition of the as-prepared $CaSr_2Al_2O_6$:0.02Eu^{3+} sample were examined using SEM and are presented in Fig. 4a. Obviously, irregular blocky particles with sizes ranging from 0.5 to 10 μm can be observed. Furthermore, the elemental distribution was studied using EDX mapping, as exhibited in Fig. 4b–f. It was found that the Ca, Sr, Al, O and Eu elements are distributed homogeneously on the surface. As expected, the EDX spectrum further proves that only the Ca, Sr, Al, O and Eu elements exist, as demonstrated in Fig. 4g. Meanwhile, to confirm whether some Eu^{2+} ions existed in the $CaSr_2Al_2O_6$:Eu^{3+} sample, the high-resolution XPS scan

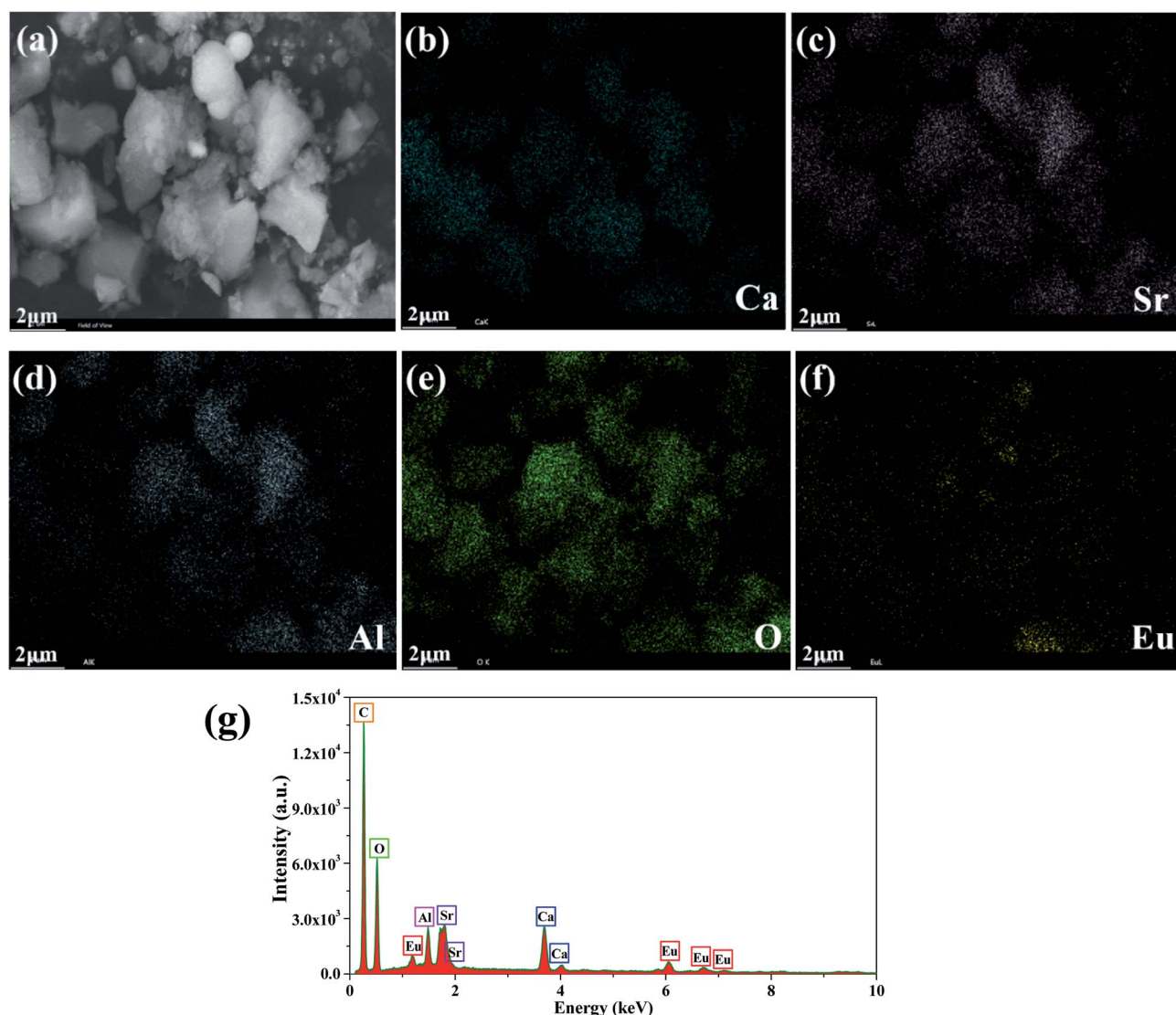**Fig. 4** (a) A representative SEM image of $CaSr_2Al_2O_6$:0.02Eu^{3+}, and the corresponding element mapping images: (b) Ca K-edge, (c) Sr L-edge, (d) Al K-edge, (e) O K-edge, and (f) Eu L-edge. (g) The EDX spectrum of $CaSr_2Al_2O_6$:0.02Eu^{3+}.

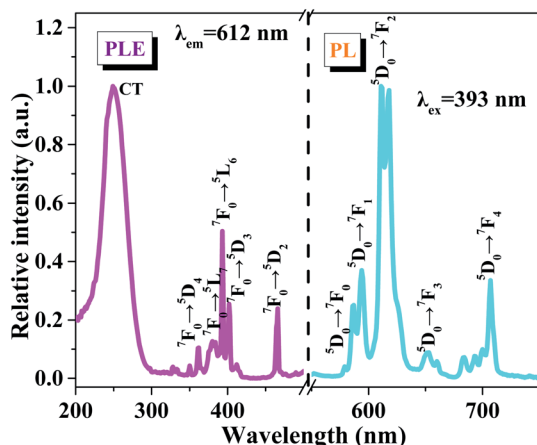Fig. 5   PLE and PL spectra of CaSr$_2$Al$_2$O$_6$:0.02Eu^{3+}.

spectrum for the Eu 4d region is shown in Fig. S2.† The presence of two peaks located at 134.4 and 141.0 eV are indicative of the Eu^{3+} 4d$_{5/2}$ and 4d$_{3/2}$ core levels, respectively, and the well-known peak around 129.4 eV associated with Eu^{2+} (4d$_{5/2}$) was not observed.[35] Therefore, there was no Eu^{2+} present in the prepared sample.

3.2   Photoluminescence properties

The PLE and PL spectra of the CaSr$_2$Al$_2$O$_6$:0.02Eu^{3+} sample are shown in Fig. 5. The broad band with a maximum at approximately 250 nm is known as the charge transfer (CT) process, which is ascribed to the transition from the O^{2-} 2p state to the Eu^{3+} 4f state. Meanwhile, the PLE spectrum contains several sharp peaks between 350 and 500 nm owing to the typical intra-4f transitions of the Eu^{3+} ions.[19,36] Obviously, the two strongest peaks at 393 and 465 nm, originating from the $^7F_0 \rightarrow {}^5L_6$ and $^7F_0 \rightarrow {}^5D_2$ transitions of the Eu^{3+} ions, respectively, can be observed, which illustrate the prepared sample can be excited by the near ultraviolet and blue LED chips effectively.[36] Upon excitation at 393 nm, several emission peaks from 550 to 750 nm, corresponding to the electronic $^5D_0 \rightarrow {}^7F_i$ ($i = 0, 1, 2, 3, 4$) transitions, are present in the PL spectrum.[3] The most

intense emission peak at 612 nm and four other weaker emission peaks at 579, 594, 653 and 707 nm can be found, which are in good agreement with the $^5D_0 \rightarrow {}^7F_2$, $^5D_0 \rightarrow {}^7F_0$, $^5D_0 \rightarrow {}^7F_1$, $^5D_0 \rightarrow {}^7F_3$ and $^5D_0 \rightarrow {}^7F_4$ transitions of the Eu^{3+} ions, respectively.[32,37,38] These results reveal that the Eu^{3+} ions have occupied a site with a narrow crystal symmetry in the lattice of CaSr$_2$Al$_2$O$_6$.

In order to investigate the influence of Eu^{3+} concentrations on the luminescent intensity, the PL spectra of the CaSr$_2$Al$_2$O$_6$:yEu^{3+} ($y = 0.005, 0.01, 0.02, 0.03, 0.04, 0.05$ and 0.10) phosphors with different Eu^{3+} ion concentrations have been measured, as shown in Fig. 6a. Clearly, all of the samples exhibit the same spectral shapes around 612 nm, except for the luminous intensities. With the increase in the concentration of Eu^{3+} ions, the emission intensity is first enhanced and then reaches the maximum at 2 mol%, and then decreases gradually owing to the concentration quenching mechanism, as demonstrated in Fig. 6b. In the CaSr$_2$Al$_2$O$_6$ matrix, the spacing between the adjacent Eu^{3+} ions will become smaller if the doping concentration of the Eu^{3+} ions reaches a certain value. Thus, the non-radiative energy transfer will increase, and then result in a decrease in the emission intensity. In general, non-radiative energy transfer occurs as an exchange interaction or electric multipole–multipole interaction from the sensitizer ions to the activator ions.[37] Among these, the exchange interaction makes a vast difference when the critical distance is less than 5 Å. Thus, the critical distance R_c between the Eu^{3+} ions is calculated according to the Blasse theory.[8] For the CaSr$_2$Al$_2$O$_6$:0.02Eu^{3+} phosphor, the values obtained were $V = 3692.4$ Å^3, $X_c = 0.02$ and $N = 48$. Therefore, the R_c was found to be 19.44 Å, which is much larger than 5 Å. Therefore, the non-radiative energy transfer between the Eu^{3+} ions is the electric multipole–multipole interaction. Herein, there are three types of electric multipole–multipole interaction, including dipole–dipole (d–d), dipole–quadrupole (d–q) and quadrupole–quadrupole (q–q) interactions, respectively. Based on Dexter's theory, the type of electric multipole–multipole interaction can be verified using the following formula:[31]

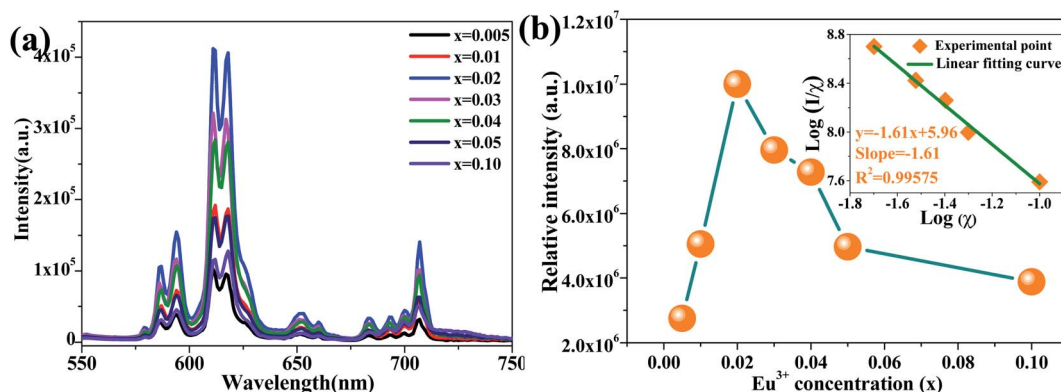$$\frac{I}{\chi} = \frac{K}{1 + \beta(\chi)^{\theta/3}} \tag{1}$$

Fig. 6   (a) PL spectra of CaSr$_2$Al$_2$O$_6$:yEu^{3+} ($y = 0.005, 0.01, 0.02, 0.03, 0.04, 0.05$, and 0.10) phosphors with different Eu^{3+} concentrations. (b) The emission intensities from $^5D_0 \rightarrow {}^7F_2$ based on various Eu^{3+} concentrations; the inset shows the fitting curve of log(I/χ) versus log(χ).

in which I corresponds to the PL emission intensity, χ represents the concentration that exceeds the optimal concentration, K and β are constants and $\theta = 6, 8,$ and 10 represent the d–d, d–q and q–q interactions, respectively. As shown in the inset of Fig. 6b, the relationship between $\log(I/\chi)$ and $\log(\chi)$ was found to be almost linear, and the slope was fitted and found to be -1.61. Therefore, the value of θ was calculated to be 4.83, which is close to 6, indicating that the concentration quenching mechanism of the Eu^{3+} ions in the $CaSr_2Al_2O_6$ phosphors is a d–d interaction.

After that, to systematically investigate the change in the luminescent intensity of the Eu^{3+} ions in the $Ca_{1+x}Sr_{2-x}Al_2O_6$ host when the Sr^{2+} ions are increasingly replaced by Ca^{2+} ions, we adjusted the molar ratio of Ca : Sr from 1 : 2 to 2 : 1. In addition, we used 2 mol% as the doped concentration of Eu^{3+} ions, which has been verified as the optimal concentration in $CaSr_2Al_2O_6$. As seen in Fig. 7a, all of the samples show the same spectral shapes with increasing Ca^{2+} concentrations (x) from 0 to 1.0. Clearly, the luminous intensities of the Eu^{3+} ions gradually increase with the enhancement of the Ca^{2+} concentrations. When x reaches 1.0, the emission intensity of the $Ca_2SrAl_2O_6$:0.02Eu^{3+} phosphor was found to be 3.55 times greater than that of the $CaSr_2Al_2O_6$:0.02Eu^{3+} phosphor, as depicted in Fig. 7b. The enhancement of the PL characteristics with the addition of Ca^{2+} may be attributed to some different factors. The bond lengths of the Ca, Sr/Ca and Sr ions coordinated with their ligands is one of the most prominent of these. Herein, the average bond lengths of Ca–O, Sr/Ca–O and Sr–O are shorter in $Ca_2SrAl_2O_6$ than those in $CaSr_2Al_2O_6$, as illustrated in Table S1.† Thus, with the increment of the Ca^{2+} doping concentrations, the average bond lengths of Ca–O, Sr/Ca–O and

Sr–O are shorter, resulting in a larger average distance between the doping elements. The larger distance will weaken the non-radiative energy transfer from one Eu^{3+} to another Eu^{3+}, and finally significantly enhance the efficiency of the radiative transition in the $Ca_2SrAl_2O_6$ host.[5,39,40] Furthermore, the Commission International de l'Eclairage (CIE 1931) chromaticity coordination diagram for the $Ca_{1+x}Sr_{2-x}Al_2O_6$:0.02Eu^{3+} phosphors is exhibited in Fig. S3.† When the value of x increases from 0 to 1.0, the CIE chromaticity coordinates shift slightly from (0.6311, 0.3684) to (0.6488, 0.3508). All of the results demonstrate that the obtained phosphors can be used as excellent red-emitting phosphors for potential applications in the field of solid-state lighting. Meanwhile, the internal quantum efficiency (IQE) of $CaSr_2Al_2O_6$:0.02Eu^{3+} and the $Ca_2SrAl_2O_6$:0.02Eu^{3+} samples were obtained and found to be 36.5% and 46.3%, respectively, which are higher than those of the commercially available phosphors Y_2O_2S:Eu^{3+} (IQE: 35%),[22] illustrating that the samples have promising application prospects in solid-state lighting.

To further verify the promoting effect of the Ca^{2+} ions on the $Ca_{1+x}Sr_{2-x}Al_2O_6$:0.02Eu^{3+} phosphors, the luminescent decay curves of $Ca_{1+x}Sr_{2-x}Al_2O_6$:0.02Eu^{3+} ($0 \leq x \leq 1.0$) were measured, as presented in Fig. 8. Obviously, all of the curves are in accordance with the following single exponential attenuation formula:[10,14]

$$I(t) = I_0 + A \exp(-t/\tau) \tag{2}$$

In which I_0 and $I(t)$ correspond to the luminescent intensities at time 0 and t, A is a constant, and τ represents the fluorescence lifetime. According to the above equation, the average lifetimes
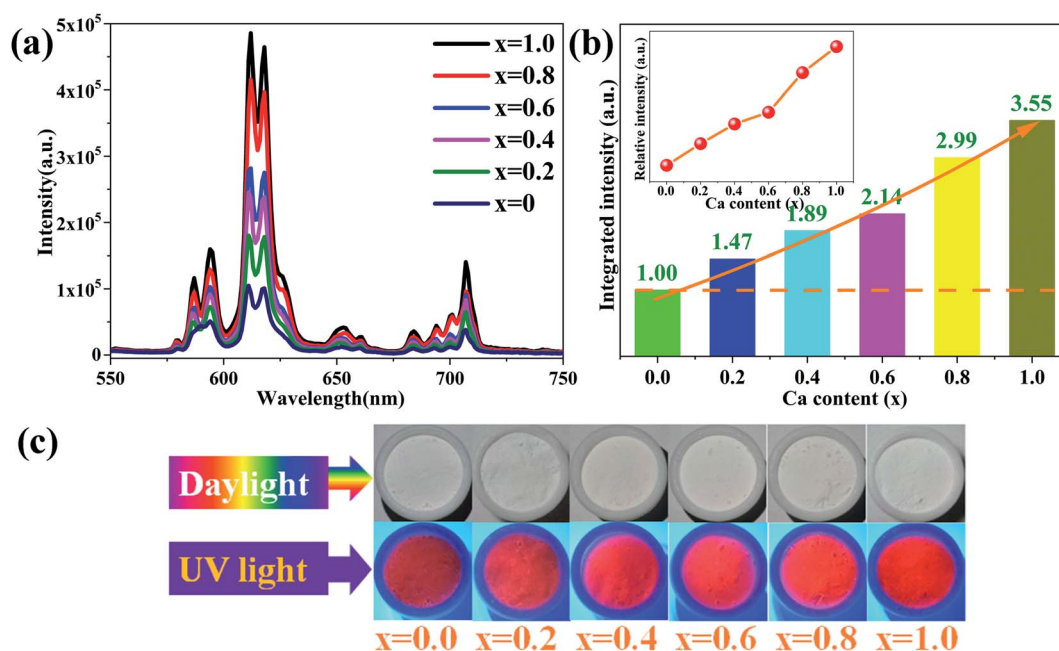

Fig. 7 (a) PL spectra of $Ca_{1+x}Sr_{2-x}Al_2O_6$:0.02Eu^{3+} ($x = 0, 0.2, 0.4, 0.6, 0.8$ and 1.0) phosphors with different Ca^{2+} concentrations. (b) Integrated emission intensities of the Eu^{3+} ions at different Ca^{2+} concentrations; the inset shows the emission intensity from $^5D_0 \rightarrow {}^7F_2$ based on different Ca^{2+} concentrations. (c) Photographs of the obtained phosphors under daylight and 365 nm UV light.

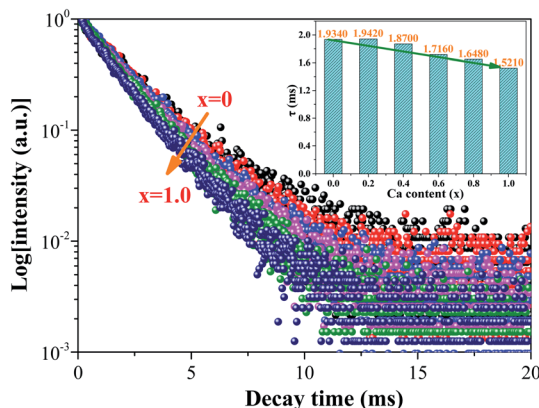**Fig. 8** The luminescent decay curves of the $Ca_{1+x}Sr_{2-x}Al_2O_6$:$0.02Eu^{3+}$ ($0 \leq x \leq 1.0$) phosphors. The inset shows the luminous lifetimes with different Ca^{2+} concentrations.

of phosphors decrease from 1.9340 to 1.5210 ms with the increase of x from 0 to 1.0. This result is mainly ascribed to the shorter average bond lengths of the Eu^{3+} ions in $Ca_2SrAl_2O_6$ compared to those in $CaSr_2Al_2O_6$.

As one of the crucial factors for the practical application of WLEDs, thermal stability has been studied systematically. The temperature-dependent PL emission spectra of the $Ca_{1+x}Sr_{2-x}$-Al_2O_6:$0.02Eu^{3+}$ phosphors with various Ca^{2+} concentrations have been shown in Fig. 9a–c. Evidently, the PL intensities of these phosphors present a slight decline as the temperature increases from 303 to 503 K. Additionally, the trend is described more clearly in Fig. 9d, in which the emission intensities decrease gradually with the increase in temperature. In particular, the PL intensity at 423 K for the $CaSr_2Al_2O_6$:$0.02Eu^{3+}$,

$Ca_{1.5}Sr_{1.5}Al_2O_6$:$0.02Eu^{3+}$ and $Ca_2SrAl_2O_6$:$0.02Eu^{3+}$ phosphors drops to 84.5%, 76.1% and 75.7% compared with the initial intensity at 303 K, respectively. All of the phosphors possess excellent thermal stability performances. Generally speaking, the rigidity of the crystal structure is an important factor for thermal stability, and superior structural rigidity can produce an excellent thermal stability.[41] As for the $Ca_{1+x}Sr_{2-x}Al_2$-O_6:$0.02Eu^{3+}$ phosphors, the rigidity of the crystal structure will be reduced if the larger Sr^{2+} ions (r = 1.18 Å, CN = 6) are replaced by smaller Ca^{2+} ions (r = 1.00 Å, CN = 6), which eventually results in a decline in the thermal stability. Subsequently, in order to further confirm the mechanism of thermal quenching, the activation energy (ΔE) of $CaSr_2Al_2O_6$:$0.02Eu^{3+}$, $Ca_{1.5}Sr_{1.5}Al_2O_6$:$0.02Eu^{3+}$ and $Ca_2SrAl_2O_6$:$0.02Eu^{3+}$ was calculated using a modified Arrhenius equation as follows:[16]

$$I_T = \frac{I_0}{1 + A\exp(-\Delta E/kT)} \tag{3}$$

Herein, I_0 and I_T correspond to the emission intensities of the initial temperature (303 K) and the given temperatures (303–503 K), respectively, A is a constant, ΔE represents the activation energy of thermal quenching and k is the Boltzmann constant. According to the equation above, the relationship of ln (I_0/I_T − 1) and $1/kT$ has been plotted and fitted in the inset of Fig. 9d. The ΔE values of $CaSr_2Al_2O_6$:$0.02Eu^{3+}$, $Ca_{1.5}Sr_{1.5}Al_2O_6$:$0.02Eu^{3+}$ and $Ca_2SrAl_2O_6$:$0.02Eu^{3+}$ were fitted and found to be 0.1189, 0.1606 and 0.1610 eV, respectively. Generally, the larger values of ΔE demonstrate that the excited state energy level locations of Eu^{3+} are much further from the conduction band, which means the thermal quenching is lower. Hence, these phosphors possess a higher ΔE compared to those of $KGd_{0.7}TiO_4$:$0.3Eu^{3+}$ (0.08 eV)[42] and $Ca_2Tb_{7.94}(SiO_4)_6O_2$:$0.06Eu^{3+}$ (0.027 eV),[43] which
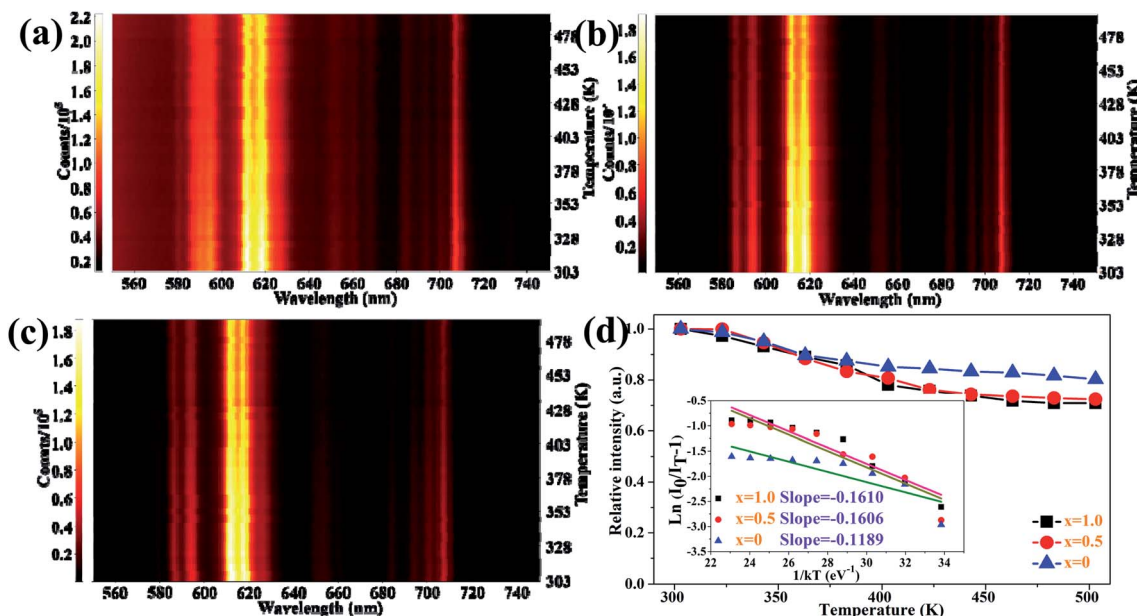
Fig. 9 The temperature-dependent PL spectra of the as-prepared $Ca_{1+x}Sr_{2-x}Al_2O_6$:$0.02Eu^{3+}$ ($0 \leq x \leq 1.0$) phosphors with various Ca^{2+} concentrations: (a) x = 0, (b) x = 0.5, and (c) x = 1.0. (d) The normalized PL intensities of the $Ca_{1+x}Sr_{2-x}Al_2O_6$:$0.02Eu^{3+}$ phosphors in the temperature range of 303 to 503 K; the inset shows the fitted curves of ln(I_0/I_T − 1) versus $1/kT$.

further demonstrates the remarkable thermal stability of the $Ca_{1+x}Sr_{2-x}Al_2O_6$:$0.02Eu^{3+}$ phosphors. In addition, the temperature-dependent luminous lifetimes of the $Ca_{1+x}Sr_{2-x}$-Al_2O_6:$0.02Eu^{3+}$ phosphors were also measured from 303 to 503 K, as shown in Fig. S5.† The fluorescence lifetimes decline to a small extent, further indicating the excellent thermal stability of these phosphors.

4. Conclusions

In conclusion, a series of novel red-emitting $CaSr_2Al_2O_6$:yEu^{3+} and $Ca_{1+x}Sr_{2-x}Al_2O_6$:$0.02Eu^{3+}$ phosphors has been successfully synthesized using a high-temperature solid-state method. The phase purities and crystal structures have been systematically investigated, and the results illustrate that all the samples possess a cubic structure system with a $Pa\bar{3}$(205) space-group. The PL spectra demonstrate that strong red emission located at 612 nm, owing to the $^5D_0 \rightarrow {}^7F_2$ transition of Eu^{3+} ions, is observed. The optimal doping concentration is 2 mol%, and the concentration quenching mechanism was determined and found to be a dipole–dipole interaction. The substitution of Sr^{2+} ions by Ca^{2+} ions can significantly increase the luminous intensities of the $Ca_{1+x}Sr_{2-x}Al_2O_6$:$0.02Eu^{3+}$ phosphors, and the emission intensity of the $Ca_2SrAl_2O_6$:$0.02Eu^{3+}$ phosphor was revealed to be 3.55 times greater than that of the $CaSr_2Al_2$-O_6:$0.02Eu^{3+}$ one. Impressively, the $Ca_{1+x}Sr_{2-x}Al_2O_6$:$0.02Eu^{3+}$ phosphors exhibit excellent thermal stability performances, and at 423 K, the PL intensities of the $CaSr_2Al_2O_6$:$0.02Eu^{3+}$, $Ca_{1.5}Sr_{1.5}Al_2O_6$:$0.02Eu^{3+}$, and $Ca_2SrAl_2O_6$:$0.02Eu^{3+}$ phosphors retain 84.5%, 76.1% and 75.7% of their intensities compared to their initial intensities at 303 K, respectively.

Conflicts of interest

There are no conflicts to decare.

Acknowledgements

References

1 M. Gao, Y. Pan, Y. Jin and J. Lin, *RSC Adv.*, 2021, **11**, 760–779.

2 Z. Xia and Q. Liu, *Prog. Mater. Sci.*, 2016, **84**, 59–117.

3 Q. Mao, B. Shen, T. Yang, J. Zhong and G. Wu, *Ceram. Int.*, 2020, **46**, 19328–19334.

4 T. Hu, Y. Gao, X. Ji, Z. Xia and Q. Zhang, *Inorg. Chem. Front.*, 2020, **7**, 2685–2691.

5 J. Yang, J. Zhang, Z. Gao, M. Tao, P. Dang, Y. Wei and G. Li, *Inorg. Chem. Front.*, 2019, **6**, 2004–2013.

6 R. J. Xie and N. Hirosaki, *Sci. Technol. Adv. Mater.*, 2016, **8**, 588–600.

7 M. G. Brik, C. Ma, A. M. Srivastava and M. Piasecki, *Chin. J. Lumin.*, 2020, **41**, 1011–1029.

8 J. Zhong, S. Zhou, D. Chen, J. Li, Y. Zhu, X. Li, L. Chen and Z. Ji, *Dalton Trans.*, 2018, **47**, 8248–8256.

9 P. Dang, G. Li, S. Liang, H. Lian and J. Lin, *J. Mater. Chem. C*, 2019, **7**, 5975–5987.

10 J. Zhong, L. Li, M. Liu, K. Wang, Y. Zhu, X. Li, Z. Ji and D. Chen, *J. Am. Ceram. Soc.*, 2019, **102**, 7376–7385.

11 Q. Wu, X. Chen, H. Chen, H. Zhang and J. Zhou, *J. Am. Ceram. Soc.*, 2019, **102**, 6068–6076.

12 W. Zhang, Y. Tong, F. Hu, R. Wei, L. Chen and H. Guo, *Ceram. Int.*, 2021, **47**, 284–291.

13 H. Chen, J. Ding, X. Ding, X. Wang, Y. Cao, Z. Zhao and Y. Wang, *Inorg. Chem.*, 2017, **56**, 10904–10913.

14 Z. Wang, Z. Wang, Y. Li, J. Liu, Q. Bao, X. Meng, K. Qiu, Z. Yang, D. Wang and P. Li, *RSC Adv.*, 2021, **11**, 2706–2717.

15 Y. Li, Y. Shi, G. Zhu, Q. Wu, H. Li, X. Wang, Q. Wang and Y. Wang, *Inorg. Chem.*, 2014, **53**, 7668–7675.

16 J. Li, J. Yan, D. Wen, W. U. Khan, J. Shi, M. Wu, Q. Su and P. A. Tanner, *J. Mater. Chem. C*, 2016, **4**, 8611–8623.

17 P. Halappa, B. Devakumar and C. Shivakumara, *New J. Chem.*, 2019, **43**, 63–71.

18 M. K. Sahu, H. Kaur, B. V. Ratnam, J. S. Kumar and M. Jayasimhadri, *Ceram. Int.*, 2020, **46**, 26410–26415.

19 M. Liu, B. Shen, K. Wang, J. Zhong and D. Chen, *RSC Adv.*, 2019, **9**, 20742–20748.

20 Y. Li, Y. Shi and Y. Wang, *ECS J. Solid State Sci. Technol.*, 2013, **2**, R208–R212.

21 X. Min, Y. Sun, L. Kong, M. Guan, M. Fang, Y. g. Liu, X. Wu and Z. Huang, *Dyes Pigm.*, 2018, **157**, 47–54.

22 D. Wen, J. Feng, J. Li, J. Shi, M. Wu and Q. Su, *J. Mater. Chem. C*, 2015, **3**, 2107–2114.

23 S. Wang, Q. Sun, B. Devakumar, B. Li, H. Guo and X. Huang, *J. Lumin.*, 2019, **206**, 571–577.

24 M. Li, J. Zhang, J. Han, Z. Qiu, W. Zhou, L. Yu, Z. Li and S. Lian, *Inorg. Chem.*, 2017, **56**, 241–251.

25 Y. Wei, L. Cao, L. Lv, G. Li, J. Hao, J. Gao, C. Su, C. C. Lin, H. S. Jang, P. Dang and J. Lin, *Chem. Mater.*, 2018, **30**, 2389–2399.

26 Y. Zhang, X. Li, K. Li, H. Lian, M. Shang and J. Lin, *ACS Appl. Mater. Interfaces*, 2015, **7**, 2715–2725.

27 J. Wan, Y. Zhang, Y. Wang, R. Ma, Y. Wu, X. Qiao and X. Fan, *J. Mater. Chem. C*, 2018, **6**, 3346–3351.

28 Y. Chen, J. He, X. Zhang, M. Rong, Z. Xia, J. Wang and Z. Q. Liu, *Inorg. Chem.*, 2020, **59**, 1383–1392.

29 M. Jiao, Y. Jia, W. Lu, W. Lv, Q. Zhao, B. Shao and H. You, *Dalton Trans.*, 2014, **43**, 3202–3209.

30 J. Zhong, D. Chen, S. Yuan, M. Liu, Y. Yuan, Y. Zhu, X. Li and Z. Ji, *Inorg. Chem.*, 2018, **57**, 8978–8987.

31 J. Zhong, Y. Peng, D. Chen, M. Liu, X. Li, Y. Zhu and Z. Ji, *J. Mater. Chem. C*, 2018, **6**, 13305–13315.

32 J. Zhao, H. Gao, H. Xu, Z. Zhao, H. Bu, X. Cao, L. He, Z. Yang and J. Sun, *RSC Adv.*, 2021, **11**, 8282–8289.

33 Q. Liu, X. Li, B. Zhang, L. Wang, Q. Zhang and L. Zhang, *Ceram. Int.*, 2016, **42**, 15294–15300.

34 C. Xia, C. Yu, M. Cao, J. Xia, D. Jiang, G. Zhou, D. Zhang and H. Li, *Ceram. Int.*, 2018, **44**, 21040–21046.

35 J. Liu, Z. Wang, X. Li, X. Meng, K. Qiu, D. Wang, J. Zhao, W. Lai, Z. Yang and P. Li, *CrystEngComm*, 2020, **22**, 5323–5337.

36 Z. Liu, C. Shen, L. Yuan, Y. Chen, L. Shen, M. He, R. Yuan, X. Liang, J. Liu and W. Xiang, *J. Am. Ceram. Soc.*, 2019, **102**, 3823–3828.

37 W. Xie, Y. Mo, C. Zou, F. Kang and G. Sun, *Inorg. Chem. Front.*, 2018, **5**, 1076–1084.

38 C. Xia, Y. Xu, M. M. Cao, Y. P. Liu, J. F. Xia, D. Y. Jiang, G. H. Zhou, R. J. Xie, D. F. Zhang and H. L. Li, *Talanta*, 2020, **212**, 120795.

39 B. Mutelet, P. Perriat, G. Ledoux, D. Amans, F. Lux, O. Tillement, C. Billotey, M. Janier, C. Villiers, R. Bazzi, S. Roux, G. Lu, Q. Gong and M. Martini, *J. Appl. Phys.*, 2011, **110**, 094317.

40 S. Saha, S. Das, U. K. Ghorai, N. Mazumder, D. Ganguly and K. K. Chattopadhyay, *J. Phys. Chem. C*, 2015, **119**, 16824–16835.

41 Q. Wang, Z. Mu, S. Zhang, X. Feng, Q. Zhang, D. Zhu, Q. Du and F. Wu, *Lumin*, 2018, **33**, 1371–1376.

42 N. Zhang, C. Guo, J. Zheng, X. Su and J. Zhao, *J. Mater. Chem. C*, 2014, **2**, 3988–3994.

43 C. Yang, S. Das and C. Lu, *J. Lumin.*, 2015, **168**, 199–206.